

LETTER TO THE EDITOR

Simulations of entropy rain-driven convection

P. J. Käpylä¹

Institute for Solar Physics (KIS), Georges-Köhler-Allee 401a, 79110 Freiburg, Germany email: pkapyla@leibniz-kis.de

April 2, 2025

ABSTRACT

Context. The paradigm of convection in solar-like stars is questioned based on recent solar observations.

Aims. The primary aim is to study the effects of surface-driven entropy rain on convection zone structure and flows.

Methods. Simulations of compressible convection in Cartesian geometry with non-uniform surface cooling are used. The cooling profile includes localized cool patches that drive deeply penetrating plumes. Results are compared with cases with uniform cooling.

Results. Sufficiently strong surface driving leads to strong non-locality and a largely subadiabatic convectively mixed layer. In such cases the net convective energy transport is done almost solely by the downflows. The spatial scale of flows decreases with increasing number of cooling patches for the vertical flows whereas the horizontal flows still peak at large scales.

Conclusions. To reach the plume-dominated regime with a predominantly subadiabatic bulk of the convection zone requires significantly more efficient entropy rain than what is realized in simulations with uniform cooling. It is plausible that this regime is realized in the Sun but that it occurs on scales smaller than those resolved currently. Current results show that entropy rain can lead to largely mildly subadiabatic convection zone, whereas its effects for the scale of convection are more subtle.

Key words. convection – turbulence – Sun:interior

1. Introduction

It has become evident during the last decade and a half that the theoretical understanding of convection in the Sun is not as complete as previously thought (e.g. [Hanasoge et al. 2010, 2012](#); [Schumacher & Sreenivasan 2020](#)). This is because helioseismology and other solar observations suggest that velocity amplitudes on large scales on the Sun are much lower than in current simulations (e.g. [Birch et al. 2024](#), and references therein). This discrepancy is commonly referred to as the convective conundrum ([O’Mara et al. 2016](#)), and it is the most likely reason why global magnetohydrodynamic simulations of the Sun struggle to reproduce the solar differential rotation and large-scale dynamo (e.g. [Käpylä et al. 2023](#), and references therein). This has led to a reevaluation of the fundamental theory of stellar convection.

In the widely used mixing length theory (e.g. [Vitense 1953](#); [Joyce & Tayar 2023](#)), convection is driven locally by an unstable temperature gradient in accordance with the Schwarzschild criterion. On the other hand, solar surface simulations (e.g. [Stein & Nordlund 1998](#)) suggest that convection in the Sun is driven by surface cooling due to a rain of low entropy material that forms strong downflow plumes. Such entropy rain is highly non-local and has been suggested to be relevant also for deep convection ([Spruit 1997](#)), and to lead to a convection zone that is weakly stably stratified ([Brandenburg 2016](#)). Recent studies of global Rossby waves in the Sun indeed suggest that the solar convection zone has to be either very nearly adiabatic ([Gizon et al. 2021](#)) or mildly subadiabatic ([Bekki 2024](#)).

Simulations of compressible convection have confirmed the existence of subadiabatic layers in the deep parts of convective envelopes (e.g. [Tremblay et al. 2015](#); [Bekki et al. 2017](#); [Hotta 2017](#); [Käpylä et al. 2017](#); [Brun et al. 2022](#); [Käpylä 2021, 2024a](#)). However, in all of these simulations the subadiabatic layer at the base of the convection zone encompasses relatively small fraction of the total depth of the convective layer. It is possible that

this is the configuration in the Sun and other stars with convective envelopes. Another possibility is that the current simulations do not capture the entropy rain originating near the surface accurately due to insufficient resolution. This is plausible because the parameter regime of the Sun is prohibitively far away from the range accessible to current simulations (e.g. [Kupka & Muthsam 2017](#); [Käpylä et al. 2023](#)). The resolution issue is particularly dire in the photosphere where the gas becomes optically thin abruptly over a distance of some tens of kilometers and coincides with the layer where entropy rain is thought to be launched. A few earlier numerical studies have explored surface effects on deep convection zone structure. For example, [Cossette & Rast \(2016\)](#) and [Yokoi et al. \(2022\)](#) found increased surface forcing, corresponding to a steeper entropy gradient, led to reduced scale of convection in deep layers. A similar approach was used in [Käpylä \(2024b\)](#) where surface forcing resulted in deeper convection zones in general due to a thermodynamics-dependent heat conductivity. On the other hand, [Hotta & Kusano \(2021\)](#) found a negligible effect of the surface layers in simulations covering the entire density contrast of the solar convection zone.

In the current study the working hypothesis is that the surface effects occur on scales that cannot be resolved directly in current simulations. Here the surface-induced entropy rain is modeled by non-uniform cooling where localized cool patches lead to plume formation. This is motivated by the non-uniform surface temperature in the Sun. A similar approach was taken by [Nelson et al. \(2018\)](#) who worked in rotating spherical shells and included a prescribed impulse to the generated plumes with the aim to study global phenomena such as differential rotation. At the other end of the spectrum are the studies of [Rast \(1998\)](#) and [Anders et al. \(2019\)](#) who studied individual plumes in a non-convecting background. Here these studies are generalized to cases with a convective background while retaining simple geometry and omitting the effects of rotation and mag-

netism. The primary aim is to explore the transition to entropy rain-dominated convection and its implications for thermal and flow structures in the convection zone.

2. The model

The model is based on that used in Käpylä (2019b, 2021, 2024a), and the PENCIL CODE (Pencil Code Collaboration et al. 2021)¹ was used to produce the simulations. The equations for compressible hydrodynamics were solved:

$$\frac{D \ln \rho}{Dt} = -\nabla \cdot \mathbf{u}, \quad (1)$$

$$\frac{D \mathbf{u}}{Dt} = \mathbf{g} - \frac{1}{\rho} (\nabla p - \nabla \cdot 2\nu \rho \mathbf{S}), \quad (2)$$

$$T \frac{Ds}{Dt} = -\frac{1}{\rho} [\nabla \cdot (\mathbf{F}_{\text{rad}} + \mathbf{F}_{\text{SGS}}) - C] + 2\nu \mathbf{S}^2, \quad (3)$$

where $D/Dt = \partial/\partial t + \mathbf{u} \cdot \nabla$ is the advective derivative, ρ is the density, \mathbf{u} is the velocity, $\mathbf{g} = -g\hat{\mathbf{e}}_z$ is the acceleration due to gravity, p is the pressure, T is the temperature, s is the specific entropy, and ν is the constant kinematic viscosity. The terms \mathbf{F}_{rad} and \mathbf{F}_{SGS} are the radiative and turbulent subgrid-scale (SGS) fluxes, respectively, and C describes cooling near the surface. \mathbf{S} is the traceless rate-of-strain tensor with $S_{ij} = \frac{1}{2}(u_{i,j} + u_{j,i}) - \frac{1}{3}\delta_{ij}\nabla \cdot \mathbf{u}$. The gas is assumed to be optically thick and fully ionized where radiation is modeled via the diffusion approximation. The ideal gas equation of state $p = (c_p - c_v)\rho T = \mathcal{R}\rho T$ applies, where \mathcal{R} is the gas constant, and c_p and c_v are the specific heats at constant pressure and volume, respectively. The radiative flux is given by $\mathbf{F}_{\text{rad}} = -K\nabla T$, where K is the radiative heat conductivity, given by $K(\rho, T) = K_0(\rho/\rho_0)^{-(a+1)}(T/T_0)^{3-b}$. The choice $a = 1$ and $b = -7/2$ corresponds to Kramers opacity law (Weiss et al. 2004), which was first used in convection simulations by Edwards (1990) and Brandenburg et al. (2000). Turbulent SGS flux $\mathbf{F}_{\text{SGS}} = -\chi_{\text{SGS}}\rho T \nabla s'$ applies to the entropy fluctuations $s'(\mathbf{x}) = s(\mathbf{x}) - \bar{s}(z)$, where the overbar indicates horizontal averaging and where χ_{SGS} is a constant. \mathbf{F}_{SGS} has a negligible contribution to the net energy flux such that $\bar{\mathbf{F}}_{\text{SGS}} \approx 0$. The cooling function C consists of two parts: uniform cooling toward a constant temperature above z_{cool} , and additional n_{patch} local patches where the cooling is applied already at a lower depth $z_{\text{patch}} < z_{\text{cool}}$. The cooling function is described in Appendix A. The advective terms in Equations (1) to (3) contain a hyperdiffusive sixth-order correction with a flow-dependent diffusion coefficient (see Appendix B of Dobler et al. 2006).

The computational domain extends between $z_{\text{bot}} \leq z \leq z_{\text{top}}$ where $z_{\text{bot}}/d = -0.45$ or $z_{\text{bot}}/d = -0.95$ depending on the model, $z_{\text{top}}/d = 1.05$, and the horizontal coordinates x and y run from $-2d$ to $2d$. The initial stratification consists of three layers. The two lower layers are polytropic with polytropic indices $n_1 = 3.25$ ($z_{\text{bot}}/d \leq z/d \leq 0$) and $n_2 = 1.5$ ($0 \leq z/d \leq 1$). The latter corresponds to a marginally stable isentropic stratification. At $t = 0$ the uppermost layer above $z/d = 1$ is isothermal, and convection ensues because the system is not in thermal equilibrium. The velocity field is perturbed with small-scale Gaussian noise with amplitude $10^{-5} \sqrt{dg}$. Horizontal boundaries are periodic, and vertical boundaries are impenetrable and stress free. A constant energy flux is imposed at the lower boundary by setting $\partial_z T = -F_{\text{bot}}/K_{\text{bot}}$, where F_{bot} is a fixed input flux and $K_{\text{bot}} = K(x, y, z_{\text{bot}})$. A constant temperature $T = T_{\text{top}}$ is imposed on the upper vertical boundary.

¹ <https://pencil-code.org>

Table 1. Summary of the zones.

Zone	\bar{F}_{conv}	$\Delta \nabla$	Label	Lower limit	Thickness
Buoyancy	> 0	> 0	BZ	z_{BZ}	d_{BZ}
Deardorff	> 0	< 0	DZ	z_{DZ}	d_{DZ}
Overshoot	< 0	< 0	OZ	z_{OZ}	d_{OZ}
Radiation	≈ 0	< 0	RZ	–	–

Notes. The bottom of the overshoot zone is taken to be where \bar{F}_{kin} falls below $10^{-2}\bar{F}_{\text{kin}}(z = z_{\text{DZ}})$ similarly as in Käpylä (2024a).

Table 2. Summary of the runs.

Run	n_{patch}	Re	z_{BZ}	z_{DZ}	z_{OZ}	d_{BZ}	d_{DZ}	d_{OZ}	d_{mix}	f_{mix}
A0	0	53	0.40	0.19	-0.06	0.59	0.21	0.25	1.06	0.44
A10	10	47	0.46	0.17	-0.20	0.54	0.28	0.37	1.19	0.55
A20	20	46	0.51	0.15	-0.21	0.48	0.36	0.37	1.21	0.60
A50	50	38	0.58	0.10	-0.42	0.40	0.48	0.52	1.40	0.71
A100	100	40	0.59	0.08	-0.43	0.37	0.52	0.50	1.39	0.73
A200	200	53	0.35	0.10	-0.21	0.61	0.25	0.31	1.17	0.48

Notes. Summary of the runs. $\text{Pr}_{\text{SGS}} = 1$ in all runs such that $\text{Pe}_{\text{SGS}} = \text{Re}$. $\text{Ra}_t = (4.4 \dots 4.6) \cdot 10^6$ in all runs, except in Run A200 where $\text{Ra}_t = 5.5 \cdot 10^6$. The values of Ra_F , and \mathcal{F}_n from the initial state at $z = 0$ are $4.9 \cdot 10^4$ and $9.1 \cdot 10^{-5}$, respectively. Runs A0, A10, and A20 have $z_{\text{bot}}/d = -0.45$ and use 288^3 grid points, whereas Runs A50, A100, and A200 have $z_{\text{bot}}/d = -0.95$ with a $288^2 \times 384$ grid.

The units of length, time, density, and entropy are given by $[x] = d$, $[t] = \sqrt{d/g}$, $[\rho] = \rho_0$, $[s] = c_p$, where ρ_0 is the initial value of density at $z = z_{\text{top}}$. The models are fully defined by choosing the values of ν , g , a , b , K_0 , ρ_0 , T_0 , and the SGS Prandtl number $\text{Pr}_{\text{SGS}} = \nu/\chi_{\text{SGS}}$, along with the parameters of the cooling function. The quantity $\xi_0 = H_p^{\text{top}}/d = \mathcal{R}T_{\text{top}}/gd = 0.054$ is the initial pressure scale height at the surface. The Prandtl number based on the radiative heat conductivity is $\text{Pr}(\mathbf{x}) = \nu/\chi(\mathbf{x})$, where $\chi(\mathbf{x}) = K(\mathbf{x})/c_p\rho(\mathbf{x})$. The dimensionless normalized flux is given by $\mathcal{F}_n(z_{\text{bot}}) = F_{\text{bot}}/\rho(z_{\text{bot}})c_s^3(z_{\text{bot}})$, where $\rho(z_{\text{bot}})$ and $c_s(z_{\text{bot}})$ are the density and the sound speed, respectively, at $z/d = -0.45$ at $t = 0$. The Rayleigh number based on the energy flux is given by $\text{Ra}_F = gd^4 F_{\text{bot}}/(c_p\rho T\nu\chi^2)$.

The Reynolds and SGS Péclet numbers are given by $\text{Re} = u_{\text{rms}}/\nu k_1$, and $\text{Pe}_{\text{SGS}} = \text{Pr}_{\text{SGS}}\text{Re} = u_{\text{rms}}/\chi_{\text{SGS}}k_1$, where u_{rms} is the rms velocity averaged over the convectively mixed layer and where $k_1 = 2\pi/d$. The total thermal diffusivity is given by $\chi_{\text{eff}}(\mathbf{x}) = \chi_{\text{SGS}} + \chi(\mathbf{x})$. The turbulent Rayleigh number $\text{Ra}_t = \frac{gd^4}{\nu\chi_{\text{eff}}} \left(-\frac{1}{c_p} \frac{d\bar{s}}{dz} \right)$ is quoted from $z/d = 0.85$ in the statistically stationary state using the temporally and horizontally averaged mean state denoted by the overbars.

3. Results

To study the structure of the convection zone, the dominant contributions to the vertical energy flux need to be identified. These are given by:

$$\bar{F}_{\text{enth}} = c_p \overline{(\rho u_z)' T'}, \quad \bar{F}_{\text{kin}} = \frac{1}{2} \overline{\rho u_z^2 u_z'}, \quad (4)$$

$$\bar{F}_{\text{rad}} = -\bar{K} \partial_z \bar{T}, \quad \bar{F}_{\text{cool}} = -\int_{z_{\text{bot}}}^z \bar{C} dz, \quad (5)$$

and correspond to convective enthalpy and kinetic energy fluxes, radiative flux and the surface cooling, respectively. Here, the

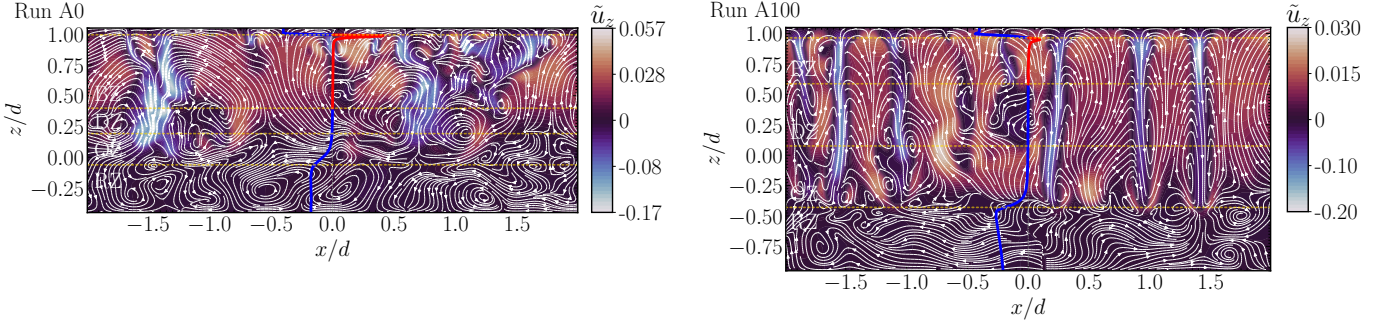


Fig. 1. Vertical slices showing the flows from Runs A0 (left) and A100 (right). Note that the box is deeper in the latter case. The colour contours indicate the vertical velocity u_z . Tilde refers to normalization by \sqrt{dg} . The arrows map streamlines where the linewidth reflects the flow speed. The blue and red curve indicated the superadiabatic temperature gradient $\Delta\nabla$ with negative (positive) values in blue (red). The boundaries of different zones defined in Table 1 are indicated by the corresponding labels and orange dotted lines.

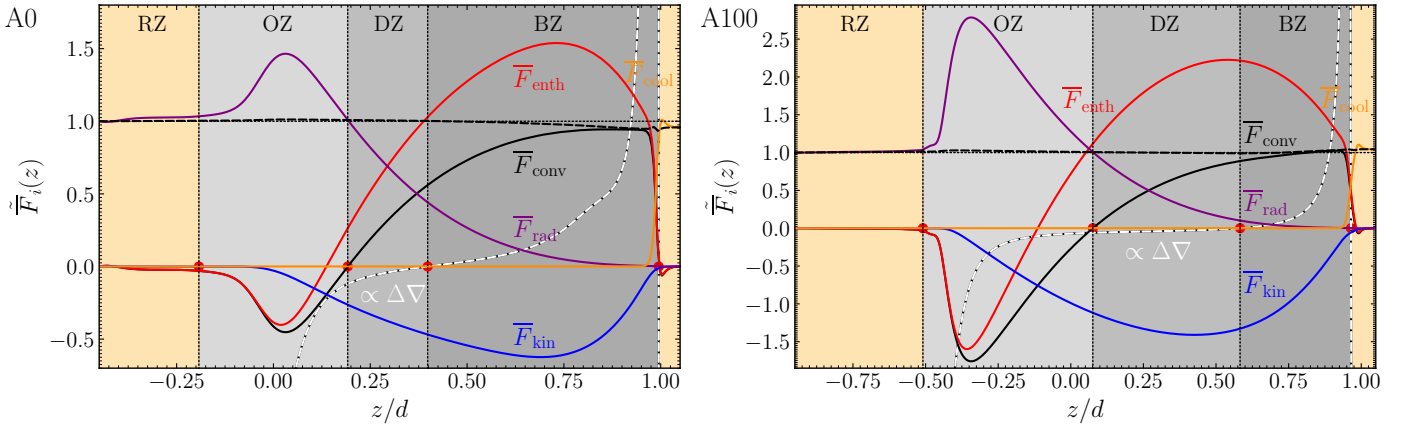


Fig. 2. Horizontally averaged energy fluxes according to Equations (4) and (5) along with \bar{F}_{conv} from runs with $n_{\text{patch}} = 0$ (Run A0) and 100 (Run A100). The dashed black and white line is proportional to $\Delta\nabla$.

primes denote fluctuations from horizontal averages. The total convected flux is $\bar{F}_{\text{conv}} = \bar{F}_{\text{enth}} + \bar{F}_{\text{kin}}$ (Cattaneo et al. 1991). Furthermore, the superadiabatic temperature gradient is $\Delta\nabla = \nabla - \nabla_{\text{ad}}$, where $\nabla = \partial \ln T / \partial \ln p$. Table 1 summarizes the different zones in the simulations based on the signs of \bar{F}_{conv} and $\Delta\nabla$. The nomenclature used here is the same as in Käpylä et al. (2017) apart from the fact that in the latter \bar{F}_{enth} instead of \bar{F}_{conv} was used in the classification.

The main objectives of the study are to determine the effect of the non-uniform entropy rain-inducing cooling on the structure of the convection zone, convective energy transport and flows in the convection zone. The runs and the most salient diagnostics are listed in Table 2.

3.1. Convection zone structure and energy transport

Figure 1 shows vertical cuts of the velocity field for runs with $n_{\text{patch}} = 0$ (Run A0) and 100 (A100). The former uses the same set-up with uniform surface cooling as in several earlier studies (e.g. Käpylä 2019b, 2021, 2024a), albeit with somewhat higher Reynolds number. This run shows a typical pattern of moderately turbulent stratified convection with cellular flows near the surface and increasing scales of convective structures in deeper layers. The many downflows near the surface around $z/d \approx 1$ merge to just a few large downflows in the deep convection zone ($z/d \approx 0.2$). This corresponds to a tree-like structure where the

trunk is situated at the base of the convection zone, and which is reminiscent of the mixing length picture of convection. In Run A100 with $n_{\text{patch}} = 100$, the structures related to large-scale cellular convection are absent and the flow is dominated by deeply penetrating downflow plumes. These downflows preserve their identity throughout the entire convection zone forming a forest-like structure. Such configuration was envisaged in the studies Spruit (1997) and Brandenburg (2016). The convectively mixed layer, consisting of BZ, DZ, and OZ, is also significantly deeper in Run A100 in comparison to Run A0 due to the deeply penetrating downflows. Figure 1 also shows that in the entropy rain-dominated regime in Run A100 the OZ and DZ are deeper, and the BZ is shallower than in the case with uniform surface cooling (Run A0).

Figure 2 shows the energy fluxes from Equations (4) and (5) from Runs A0 and A100. Similar plots for the other runs are shown in Appendix B. A particularly striking result is the increasing depth of the DZ and OZ when n_{patch} is increased. Table 2 lists the depths of different zones for all of the current simulations. The depth of BZ decreases, and the depth of DZ increases up to $n_{\text{patch}} = 100$, whereas OZ is already somewhat shallower in Run A50 in comparison to Run A100. In the extreme case of $n_{\text{patch}} = 200$ (Run A200), the zone structure is again approaching that of Run A0 without cooling patches. The most likely reason is plume merging and the fact that even a small anisotropy in the placing of cooling patches leads to horizontal pressure gradients that can drive large-scale circulation.

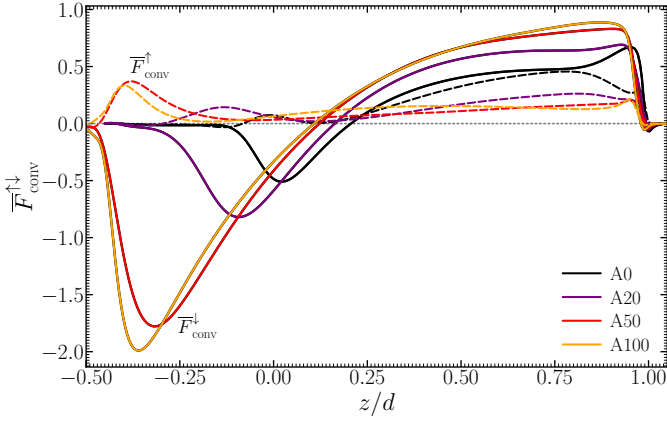


Fig. 3. Net convected flux from downflows ($\bar{F}_{\text{conv}}^{\downarrow}$, solid lines) and upflows ($\bar{F}_{\text{conv}}^{\uparrow}$, dashed lines) from representative runs indicated by the legend.

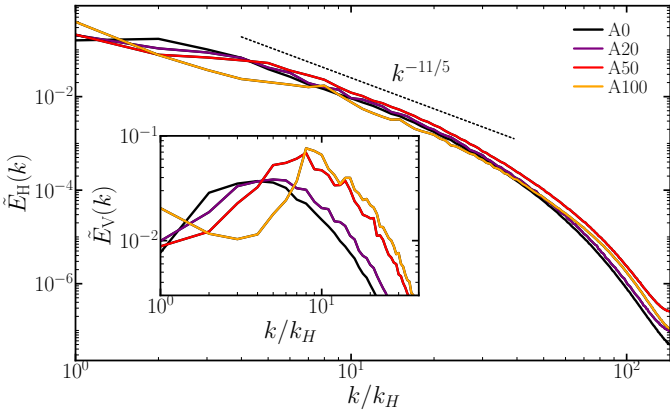


Fig. 4. Power spectra of horizontal flows $E_H(k)$ from the same runs as in Figure 3 from $z/d = 0.85$. Bolgiano-Obukhov $k^{-11/5}$ scaling is shown for reference. The inset shows the power spectrum of vertical flows $E_V(k)$ for $k/k_H < 40$ for the same runs. Tildes refer to normalization by the integrated spectrum for each case.

The last two columns of Table 2 list the depth of the convectively mixed layer $d_{\text{mix}} = d_{\text{BZ}} + d_{\text{DZ}} + d_{\text{OZ}}$ and the fraction of d_{mix} which is stably stratified according to the Schwarzschild criterion, $f_{\text{mix}} = (d_{\text{DZ}} + d_{\text{OZ}})/d_{\text{mix}}$. Even in Run A0 with no cooling patches, over 40 per cent of the convectively mixed layer is stably stratified. This fraction increases to 73 per cent in Run A100, in which case only about a quarter of the convectively mixed layer would be considered convective in the classical mixing length paradigm.

The increasing depth of the subadiabatic regions is associated with boosted magnitudes of the convective enthalpy flux \bar{F}_{enth} and the kinetic energy flux \bar{F}_{kin} . In Runs A50 and A100 the maximum of \bar{F}_{enth} is nearly twice F_{bot} and the maxima of $|\bar{F}_{\text{kin}}|$ is roughly $1.3F_{\text{bot}}$; see Figs. 2 and B.1. The latter indicates a significant increase in the energy transport due to downflows. Figure 3 shows the net convected flux (\bar{F}_{conv}) separately for downflows and upflows for representative runs. In the fiducial Run A0 the upflows and downflows transport roughly equal amounts of flux in the bulk of the CZ between $0.2 \lesssim z/d \lesssim 0.8$. When n_{patch} increases, the share of the net energy flux carried by the downflows increases such that for $n_{\text{patch}} = 50$ (Run A50)

and $n_{\text{patch}} = 100$ (Run A100) the upflows contribute only about $0.2F_{\text{bot}}$ whereas the downflows transport the majority of the flux with $0.8F_{\text{bot}}$. For $n_{\text{patch}} = 200$ the flux balance resembles more the case with no plumes because large-scale convection ensues in this case; see Figure B.1.

3.2. Spatial scale of convection

The power spectrum of horizontal velocities $E_H(k)$ at $z/d = 0.85$ from representative runs are shown in Figure 4. The maximum of $E_H(k)$ is at the largest possible scale irrespective of the boundary forcing. This is likely due to the aforementioned sensitivity to the placement of the cooling patches leading to horizontal pressure gradients that drive flows possibly on very large scales. This is especially an issue in the cases studied here where the cooling patches are stationary. On intermediate scales ($5 \lesssim k/k_H \lesssim 40$) the power spectra for the horizontal flows is close to the Bolgiano-Obukhov $k^{-11/5}$ scaling similarly to Käpylä (2021) and Warnecke et al. (2024). The peak of the power spectrum of vertical flows ($E_V(k)$) shifts toward smaller scales (higher k) as n_{patch} increases, reflecting the dominance of the plumes for vertical flows. In Figure 4 normalization is chosen such that differences between runs appear in the shape of the spectra. An alternative presentation highlighting the absolute differences between runs is shown in Appendix C.

4. Conclusions

The current proof-of-concept simulations show that strong entropy rain can radically change the convective flows and the ensuing energy transport as well as the thermal structure of the convection zone. In the entropy rain-dominated regime convection is dominated by downflows plumes penetrating the whole convection zone rendering the majority of the convectively mixed layer weakly stably stratified along the pioneering ideas of Spruit (1997) and Brandenburg (2016). The idea of entropy rain-dominated convection in the Sun coincides with the recent studies of solar Rossby waves that suggest weak subadiabaticity of deep convection zone (Bekki 2024) and possible fast small-scale downflows at supergranular scales (Hanson et al. 2024).

The current simulations employ a very simple setup and probe a very modest portion of the presently accessible parameter space. Furthermore, rotation and magnetic fields, that are dynamically important in stellar interiors, are neglected. Although a recent study (Käpylä 2024a) suggests that convection in the Sun is not strongly rotationally constrained anywhere, its effect is perhaps more subtle in the entropy rain-dominated regime because the slow and spatially larger upflows are much more affected by rotation than the fast and small downflows. The increasing anisotropy between upflows and downflows can also have implications also for large-scale magnetic field generation due to convection. The nonlinear backreaction of small-scale magnetic fields on convection (Hotta et al. 2022), is another aspect that cannot in general be neglected. These effects will be explored further in future studies.

Acknowledgements. I acknowledge the stimulating discussions with participants of the Nordita Scientific Program on “Stellar Convection: Modelling, Theory and Observations”, in August and September 2024 in Stockholm. The simulations were performed using the resources granted by the Gauss Center for Supercomputing for the Large-Scale computing project “Cracking the Convective Conundrum” in the Leibniz Supercomputing Centre’s SuperMUC-NG supercomputer in Garching, Germany.

References

- Anders, E. H., Lecoanet, D., & Brown, B. P. 2019, *ApJ*, 884, 65
- Bekki, Y. 2024, *A&A*, 682, A39
- Bekki, Y., Hotta, H., & Yokoyama, T. 2017, *ApJ*, 851, 74
- Birch, A. C., Proxauf, B., Duvall, T. L., et al. 2024, *Physics of Fluids*, 36, 117136
- Brandenburg, A. 2016, *ApJ*, 832, 6
- Brandenburg, A., Nordlund, A., & Stein, R. F. 2000, in *Geophysical and Astrophysical Convection, Contributions from a workshop sponsored by the Geophysical Turbulence Program at the National Center for Atmospheric Research, October, 1995*. Edited by Peter A. Fox and Robert M. Kerr. Published by Gordon and Breach Science Publishers, The Netherlands, 2000, p. 85-105, ed. P. A. Fox & R. M. Kerr, 85–105
- Brun, A. S., Strugarek, A., Noraz, Q., et al. 2022, *ApJ*, 926, 21
- Cattaneo, F., Brummell, N. H., Toomre, J., Malagoli, A., & Hurlburt, N. E. 1991, *ApJ*, 370, 282
- Cossette, J.-F. & Rast, M. P. 2016, *ApJ*, 829, L17
- Dobler, W., Stix, M., & Brandenburg, A. 2006, *ApJ*, 638, 336
- Edwards, J. M. 1990, *MNRAS*, 242, 224
- Gizon, L., Cameron, R. H., Bekki, Y., et al. 2021, *A&A*, 652, L6
- Hanasoge, S. M., Duvall, Thomas L., J., & DeRosa, M. L. 2010, *ApJ*, 712, L98
- Hanasoge, S. M., Duvall, T. L., & Sreenivasan, K. R. 2012, *Proc. Natl. Acad. Sci.*, 109, 11928
- Hanson, C. S., Bharati Das, S., Mani, P., Hanasoge, S., & Sreenivasan, K. R. 2024, *Nature Astronomy*, 8, 1088
- Hotta, H. 2017, *ApJ*, 843, 52
- Hotta, H. & Kusano, K. 2021, *Nature Astronomy*, 5, 1100
- Hotta, H., Kusano, K., & Shimada, R. 2022, *ApJ*, 933, 199
- Joyce, M. & Tayar, J. 2023, *Galaxies*, 11, 75
- Käpylä, P. J. 2019a, *Astronomische Nachrichten*, 340, 744
- Käpylä, P. J. 2019b, *A&A*, 631, A122
- Käpylä, P. J. 2021, *A&A*, 655, A78
- Käpylä, P. J. 2024a, *A&A*, 683, A221
- Käpylä, P. J. 2024b, in *IAU Symposium, Vol. 365, IAU Symposium*, ed. A. V. Getling & L. L. Kitchatinov, 5–15
- Käpylä, P. J., Browning, M. K., Brun, A. S., Guerrero, G., & Warnecke, J. 2023, *Space Sci. Rev.*, 219, 58
- Käpylä, P. J., Rheinhardt, M., Brandenburg, A., et al. 2017, *ApJ*, 845, L23
- Kupka, F. & Muthsam, H. J. 2017, *Liv. Rev. Comp. Astrophys.*, 3, 1
- Nelson, N. J., Featherstone, N. A., Miesch, M. S., & Toomre, J. 2018, *ApJ*, 859, 117
- O'Mara, B., Miesch, M. S., Featherstone, N. A., & Augustson, K. C. 2016, *Adv. Space Res.*, 58, 1475
- Pencil Code Collaboration, Brandenburg, A., Johansen, A., et al. 2021, *The Journal of Open Source Software*, 6, 2807
- Rast, M. P. 1998, *Journal of Fluid Mechanics*, 369, 125
- Schumacher, J. & Sreenivasan, K. R. 2020, *Reviews of Modern Physics*, 92, 041001
- Spruit, H. 1997, *Mem. Soc. Astron. Italiana*, 68, 397
- Stein, R. F. & Nordlund, Å. 1998, *ApJ*, 499, 914
- Tremblay, P.-E., Ludwig, H.-G., Freytag, B., et al. 2015, *ApJ*, 799, 142
- Vitense, E. 1953, *ZAp*, 32, 135
- Warnecke, J., Korpi-Lagg, M. J., Rheinhard, M., Viviani, M., & Prabhu, A. 2024, arXiv e-prints, arXiv:2406.08967
- Weiss, A., Hillebrandt, W., Thomas, H.-C., & Ritter, H. 2004, *Cox and Giuli's Principles of Stellar Structure* (Cambridge, UK: Cambridge Scientific Publishers Ltd)
- Yokoi, N., Masada, Y., & Takiwaki, T. 2022, *MNRAS*, 516, 2718

Appendix A: Cooling function

The cooling near the surface is described by two parts

$$C = C_1 + C_2, \quad (\text{A.1})$$

where

$$C_1 = \rho c_P \frac{T_{\text{cool}} - T}{\tau_{\text{cool1}}} f_{\text{cool}}(z, z_{\text{cool}}), \quad (\text{A.2})$$

where $\tau_{\text{cool1}} = 0.2 \sqrt{d/g}$ is a cooling time, $T = e/c_V$ is the temperature, e is the internal energy, and $T_{\text{cool}} = T_{\text{top}}$ is a reference temperature corresponding to the fixed value at the top boundary. Furthermore,

$$f_{\text{cool}}(z, z_{\text{cool}}) = \frac{1}{2} \left[1 + \tanh \left(\frac{z - z_{\text{cool}}}{d_{\text{cool}}} \right) \right], \quad (\text{A.3})$$

where $z_{\text{cool}}/d = 1$ and $d_{\text{cool}} = 0.01d$ for C_1 .

In addition, n_{patch} localized cooling patches are introduced via C_2 . Each patch follows:

$$C_2 = \rho c_P \frac{T_{\text{cool}} - T}{\tau_{\text{cool2}}} f_{\text{cool}}(z, z_{\text{patch}}) \times \exp \left(-\frac{1}{2} \frac{(x - x_{\text{patch}})^2 + (y - y_{\text{patch}})^2}{d_{\text{patch}}^2} \right), \quad (\text{A.4})$$

where $\tau_{\text{cool2}} = 0.067 \sqrt{d/g}$, f_{cool} is the same profile as above with $z_{\text{patch}}/d = 0.96$, and where the width of the patches is $d_{\text{patch}} = 0.05d$. Since $z_{\text{patch}} < z_{\text{cool}}$, the localized cooling corresponds to cool fingers penetrating the upper part of the convection zone. The number of patches (n_{patch}) is another input to the models. In the present study the positions $(x_{\text{patch}}, y_{\text{patch}})$ of the patches are fixed in time and chosen such that $\sum_i^{n_{\text{patch}}} x_{\text{patch}}^{(i)} = 0$ and $\sum_i^{n_{\text{patch}}} y_{\text{patch}}^{(i)} = 0$.

Appendix B: Energy fluxes

Figure B.1 shows the energy fluxes from Runs A10, A20, A50, and A200.

Appendix C: Power spectra and anisotropy

The horizontal and vertical power spectra are defined such that

$$\int_0^{k_{\text{max}}} E_V(k, z) dk = \frac{1}{2} \overline{u_z^2}(z), \quad (\text{C.1})$$

$$\int_0^{k_{\text{max}}} E_H(k, z) dk = \frac{1}{2} [\overline{u_x^2}(z) + \overline{u_y^2}(z)]. \quad (\text{C.2})$$

Figure B.2 shows the vertical and horizontal spectra from the same runs as in Figure 4 but normalized with respect to the integrated spectra in Run A0. Both the vertical and horizontal velocities decrease with n_{patch} . The anisotropy of the flow can be characterized with the vertical spectral anisotropy parameter (Käpylä 2019a):

$$A_V(k, z) = \frac{E_H(k, z) - 2E_V(k, z)}{E_K(k, z)}, \quad (\text{C.3})$$

where $E_K(k, z) = E_H(k, z) + E_V(k, z)$. The anisotropy parameter is shown in Figure B.3 from $z/d = 0.49$ which is near the middle of the convectively mixed layer. While the anisotropy at large scales is weak irrespective of n_{patch} , it is significantly enhanced at intermediate and small scales ($k/k_H \gtrsim 7$). The increased anisotropy parallels the increasing dominance of downflows in the energy transport.

A further diagnostic of the asymmetry of convective flows is the filling factor of downflows f^\downarrow , defined via

$$\overline{u}_z = f^\downarrow \overline{u}_z^\downarrow + (1 - f^\downarrow) \overline{u}_z^\uparrow, \quad (\text{C.4})$$

where $\overline{u}_z^\downarrow$ and \overline{u}_z^\uparrow are the averaged downflows and upflows, respectively. Figure B.4 shows that the filling factor decreases monotonically everywhere when more downflow plumes are added until $n_{\text{patch}} = 50$. This can be understood such that in cases with many plumes, cellular convection is excited only near the surface whereas deeper down the average stratification is stably stratified and plumes are almost the only downflow structures. For $n_{\text{patch}} = 100$ (Run A100) the spatial profile of f^\downarrow changes although it is still on average lower than for the cases with fewer

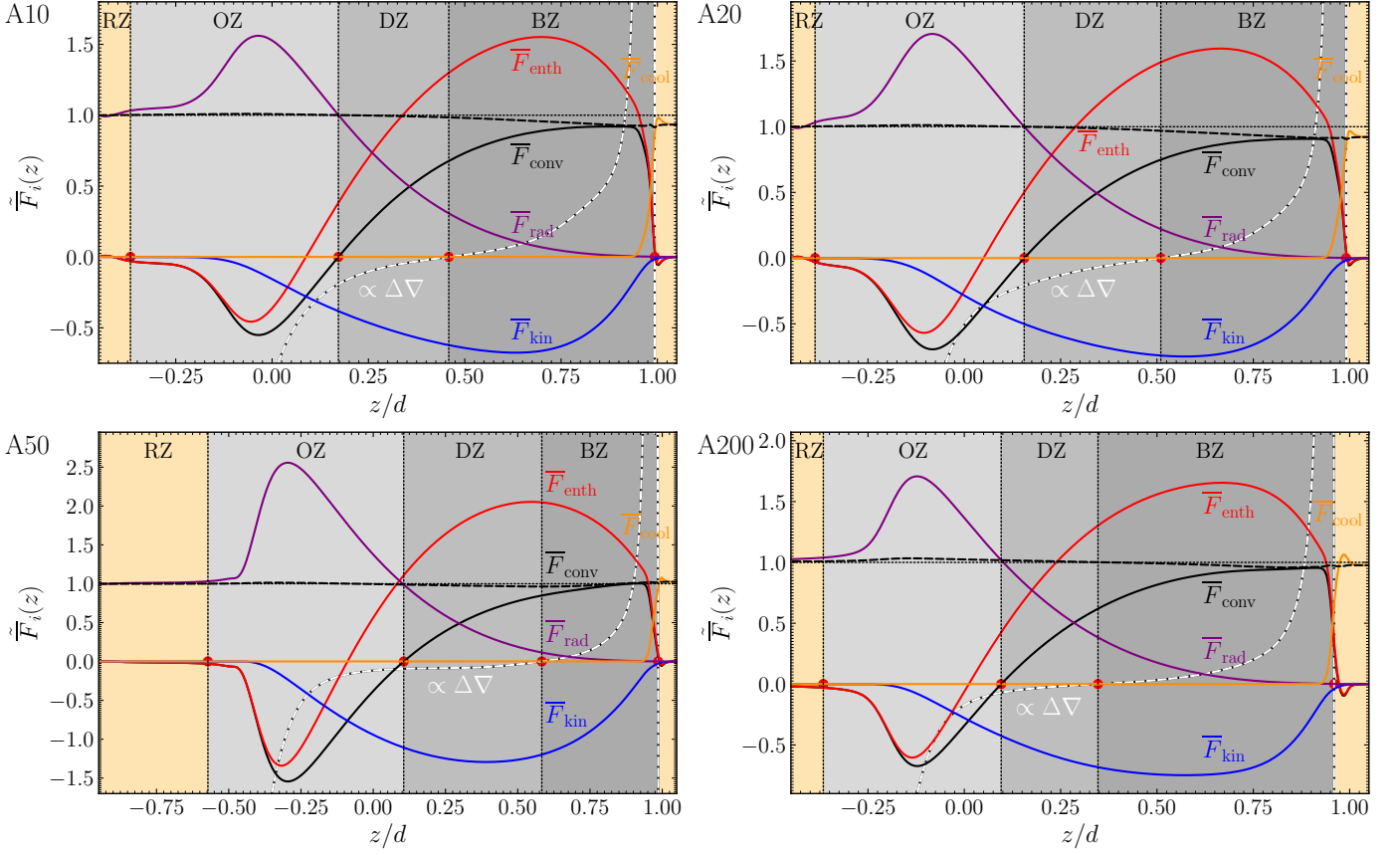


Fig. B.1. Horizontally averaged energy fluxes according to Equations (4) and (5) along with $\overline{F}_{\text{conv}}$ from runs with $n_{\text{plume}} = 10, 20, 50,$ and 200 .

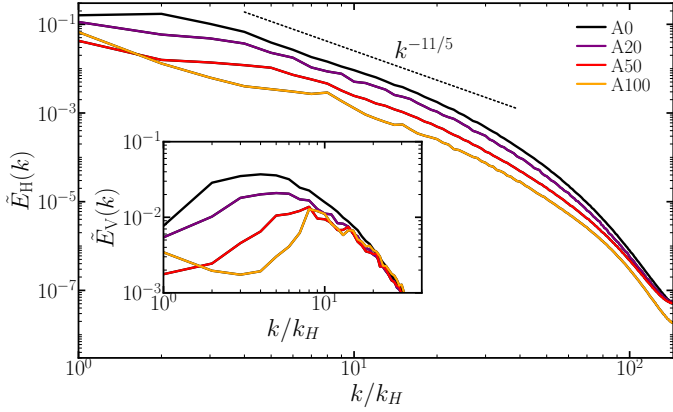


Fig. B.2. Same as Figure 4 but normalization with respect to the integrated spectra of Run A0.

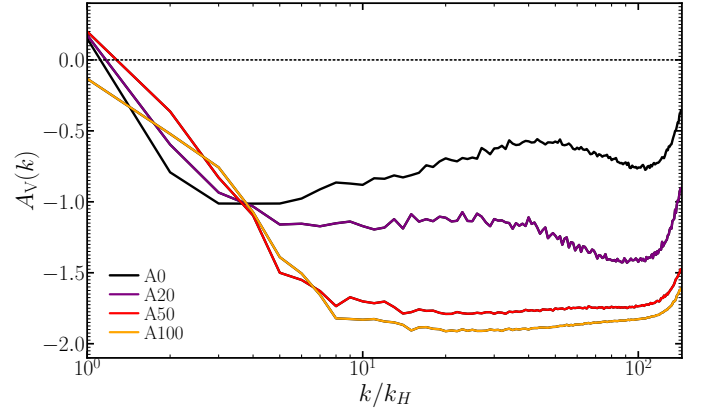


Fig. B.3. Anisotropy parameter $A_V(k)$ from the same runs as in Figure 4.

plumes. For $n_{\text{patch}} = 200$ (Run A200) the filling factor is again similar to the cases with few or no imposed plumes. This is explained by merging of plumes already near the surface into larger downflows and the development of large-scale overturning convection in that case.

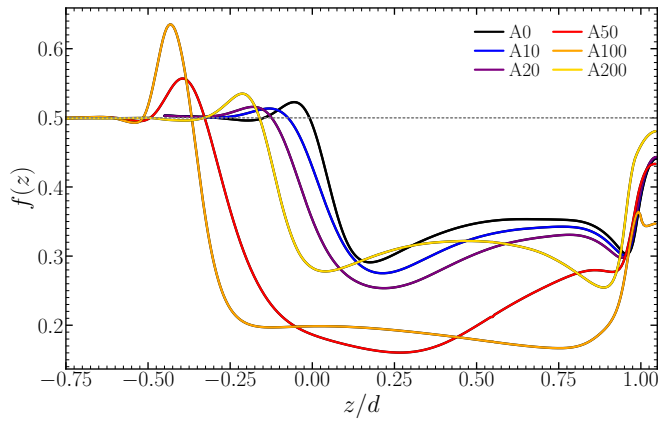


Fig. B.4. Filling factor of downflows as a function of depth from all of the current runs.